



Electrolytic Etching of Germanium Substrates with Hydrogen Peroxide

Joseph G. Wood, Luke van Buuren, Ziang Guo, Ece Deniz, Marina S. Leite, Arthur C. Carpenter, Charles E. Hunt, and Klaus van Benthem,

Department of Materials Science and Engineering, University of California, Davis, Davis, California, United States of America Department of Electrical and Computer Engineering, University of California, Davis, Davis, California, United States of America Lawrence Livermore National Laboratory, Livermore, California 94550, United States of America

Anodic electrolytic etching of germanium has been performed in hydrogen peroxide etchants with controlled external conditions. In-situ current and ex-situ etch-depths were measured and tracked with respect to etchant composition and stir rates. Gas bubbles formed during the etching process were found to cause non-uniformity in etch-current and surface quality. The effects were minimized in specific composition spaces. Quantitative analysis revealed a linear correlation of the number of electrons transferred during germanium oxidation with the number of surface atoms removed. Experimental results of 2.77 electrons/atom deviate significantly from 4 electrons/atom previously reported for silicon. The conclusion is that etching mechanisms for germanium are sufficiently different from those for silicon which invalidates the direct transfer of processing techniques between the two materials.

© 2023 The Author(s). Published on behalf of The Electrochemical Society by IOP Publishing Limited. This is an open access article distributed under the terms of the Creative Commons Attribution Non-Commercial No Derivatives 4.0 License (CC BY-NC-ND, http://creativecommons.org/licenses/by-nc-nd/4.0/), which permits non-commercial reuse, distribution, and reproduction in any medium, provided the original work is not changed in any way and is properly cited. For permission for commercial reuse, please email: permissions@ioppublishing.org. [DOI: 10.1149/1945-7111/ad0076]

Manuscript submitted August 25, 2023; revised manuscript received September 26, 2023. Published October 13, 2023.

Supplementary material for this article is available online

Recent advancements in homoepitaxially-grown germanium result in unprecedented low defect densities and incur interest in germanium as an alternative for next-generation backside imagers. Compared to silicon, germanium is characterized by a smaller bandgap, improved X-ray and infrared photon absorption, and increased carrier mobilities. These advantages favor germanium towards high throughput applications, such as high-speed hard X-ray imaging. Appreciable absorption in the near-infrared regime, where silicon is essentially transparent, makes germanium ideally suited for use in light detection and ranging (LiDAR) and photovoltaic systems. Appreciable absorption in the near-infrared regime, where silicon is essentially transparent, and photovoltaic systems.

The fabrication of backside imagers requires the removal of the substrate utilized for homoepitaxial growth, which is typically accomplished by selective etching. Chemical etching techniques used for silicon cannot be directly applied to germanium due to different electronegativity and more complex oxidation behavior. $^{5-7}$ Unlike silicon, germanium oxidizes as a mix of glassy GeO₂, GeO, and Ge₂O₃. GeO₂ is both hygroscopic and water-soluble, leading to rapid device degradation when exposed to humidity, and decomposes to GeO, which is volatile at temperatures above 400 °C. $^{8-13}$

Etching of germanium is an electrochemical redox reaction in which a germanium oxide complex is formed and subsequently dissolved. The etchant must be composed of an oxidizing agent and a dissolution agent. Water can perform both roles but etches at a relatively low rate. More vigorous oxidizing agents include hydrogen peroxide and nitric acid. Dissolution agents can be acids, including, for instance, hydrofluoric acid, phosphoric acid, sulfuric acid, hydrochloric acid, or bases, such as sodium hydroxide. 13 Earlier etching studies for germanium have been limited to surface preparation or shallow etching.^{7,13,14} More recently deep planar etching was accomplished with combinations of sulfuric acid with hydrogen peroxide, and hydrofluoric acid with nitric acid. While achieving several hundred microns of isotropic etching with minimal surface roughness, ^{16,17} etch rates and the nondiscriminatory nature of these etchants make them less suitable for selective etching. During the fabrication of backside imagers, precise control for deep etching is required to avoid damaging active device layers. For silicon-based technologies, heavily doped sacrificial layers are used as effective etch-stops.6 The original etch stop/substrate interface

ideally results in a uniformly etched surface. Etch selectivity as a figure of merit is the ratio of etch-rates between two adjacent materials. Divan et al. used ion implantation to dope germanium wafers and reported an etch-selectivity of 100 for an acid-based etchant of $\rm H_3PO_4:H_2O2:C_2H_5OH$ (1:1:1 or 1:1:3 by volume). However, ion implantation caused inhomogeneous dopant distributions resulting in anisotropic etching and significant surface pitting. These effects are detrimental to photodiodes because of premature recombination of holes and electrons that will reduce quantum efficiency. Additionally, defects can serve as charge centers within the device, alter the path of charge carriers, and degrade the signal response.

This study reports electrolytic etching of germanium in water/ hydrogen peroxide mixtures as a function of solution additives and stirring. Hydrogen peroxide offers a safe, simple, inexpensive system to study with a broad background of existing data for comparison. ^{19,20} A custom-designed electrolytic etch cell was constructed to optimize the etch process. The experimental results demonstrate a linear correlation between the charge transfer during the oxidation reaction and the number of atoms removed from the germanium surface.

Experimental

Materials preparation.—Commercially available single crystal-line germanium wafers (p-type, undoped, >50 ohm-cm, MTI Corporation, Richmond, CA) were diced into 14 mm × 14 mm squares in a clean room. Polished (100) surfaces were cleaned under sonication in alternating baths of acetone, deionized (DI) water, and methanol. After rapid blow-drying the cleaned surfaces were specular.

All etchant solutions had a volume of 102 ml and were composed of 30% hydrogen peroxide (electronic grade) and DI water (\sim 16 M Ω – cm) with a ratio of 6:12 by volume. In select experiments DI water was partly replaced by tertbutyl alcohol (TBA). Sodium phosphate monobasic monohydrate (MSP) was added to stabilize hydrogen peroxide. Concentrations of TBA and MSP were systematically modified between 0 ml and 12 ml and 0 g and 10 g, respectively.

Etching procedures.—Etch experiments were carried out with the custom-built electrolytic etch cell represented in Fig. 1. The two-electrode etch cell consists of a polytetrafluoroethylene (PTFE)

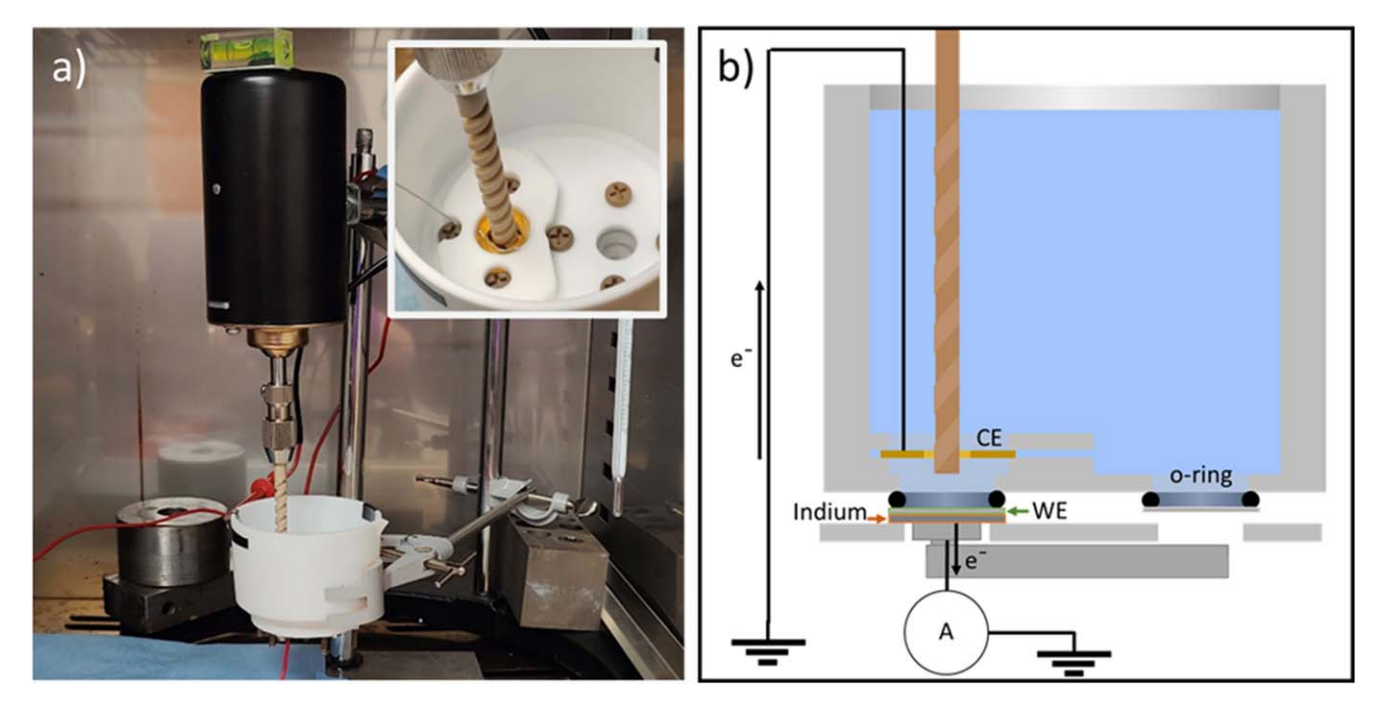


Figure 1. (a) Etch cell mounted inside low temperature furnace. Inset: top-down view the inner beaker showing the position of the electrode and stir rod. (b) Cross-sectional diagram showing the arrangement of the electrochemical circuit.

beaker to hold the electrolyte solution, a gold counter electrode (CE), and a germanium sample mounted at the bottom of the beaker which serves as the working electrode (WE). An indium plate was pressed against the backside of the germanium wafer to create an ohmic contact between germanium and the power supply.

During select experiments the etchant was stirred with a 0.635 cm diameter polyetheretherketone rod with two 45° helix flutes. The stir rod was inserted into the etch cell, positioned through a hole in the CE, and placed directly above the surface of the germanium samples. The rotation of the stirrer creates downward momentum of the etchant, forcing flow towards and across the wafer surface. The stir speed was controlled by varying the current supplied by the attached DC power source. Rotation speeds up to 2700 rpm were measured and calibrated (see Fig. S1 in supplemental materials).

The etch cell was placed into a low-temperature furnace to ensure temperature stability. All experiments were performed at a constant set temperature of 25 $^{\circ}$ C. The furnace was sealed to exclude ambient light.

The CE was directly grounded while the WE was connected to ground through a Fluke 289 multimeter, which recorded current as a function of time at 2 s intervals. After 30 s the etchant was added, and the stir rod was started. After 120 min the etchant was drained, and the beaker was thoroughly rinsed with DI water. The sample was then suspended in acetone to arrest any residual etching. Some experiments were performed outside the furnace to enable in situ observation by optical microscopy under minimal ambient light.

Characterization.—After experiments concluded, topography profiles of the etched surfaces were determined with a Bruker Dektak XT 2D contact profilometer. Profiles were recorded along each diagonal of the samples as displayed by the inset in Fig. 2. Profilometer scans were approximately 17 mm long and extended over unetched regions on both sides of the etch well for subsequent calibration and fitting (see Fig. 2). Raw data collected from the profilometer exhibited curvature that is attributed to the mechanical motion of the stage. To correct for this systematic error, data recorded from unetched regions were fitted with a 4th-order polynomial function with constant positive concavity. Prior to each profilometer scan, a standard reference was used for calibration.

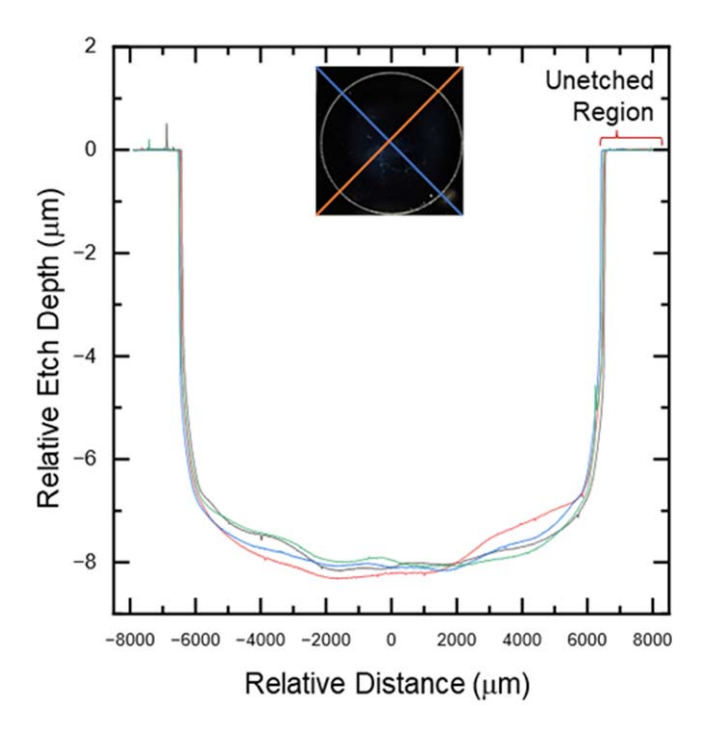


Figure 2. Profilometer scans of a specular etched wafer. The maximum etch depth is $\sim 8.17~\mu m$. The left and right flat portions represent unetched regions used to fit the scan curvature. Inset: scan directions overlayed on wafer image.

An effective etch volume was calculated from each topography scan and volumes were averaged for each sample. From the effective etch-volumes, equivalent etch-depths were calculated using cylindrical volumes with a diameter equal to the measured diameter of the etch well. The calculated depths reported below are therefore based on the assumption of a radially isotropic etch well.

Etched surfaces were examined under high vacuum with a Thermo Fisher Quattro S Environmental Scanning Electron Microscope (ESEM, Thermo Fisher, Hillsboro, OR) operated at 15 keV. Electron

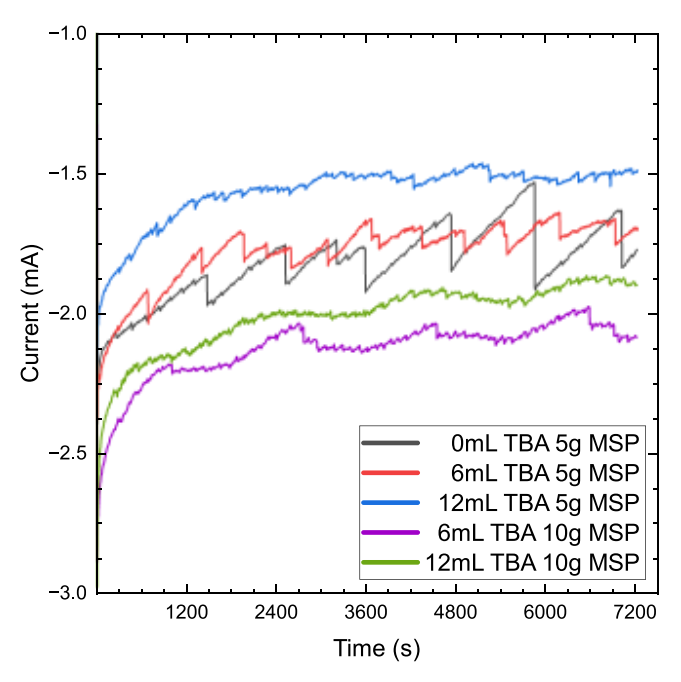


Figure 3. Measured current as a function of elapsed etch time for different additions of TBA. Negative current indicates electron flow from the positively biased WE towards the negatively biased CE.

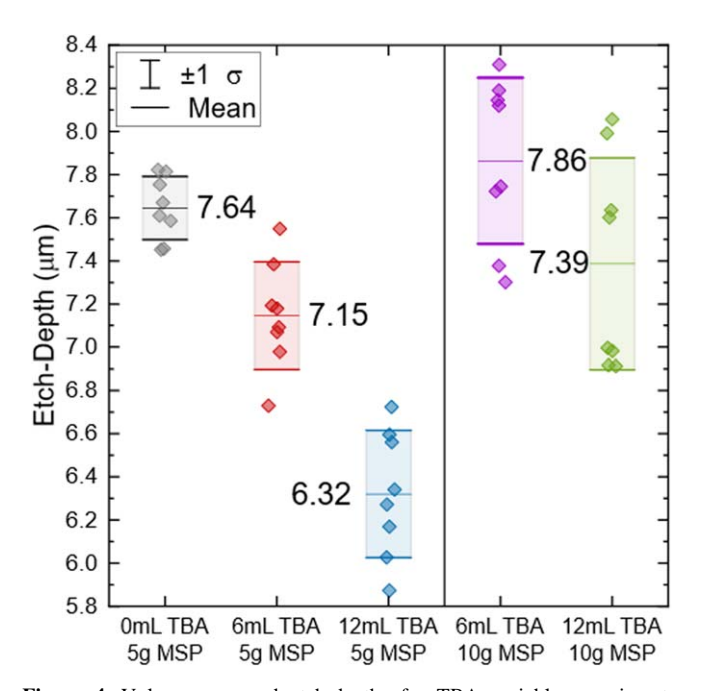


Figure 4. Volume averaged etch-depths for TBA variable experiments. Plots divided by MSP mass. σ denotes one standard deviation.

micrographs were recorded with an Everhart–Thornley detector. Surface topography was also characterized by atomic force microscopy (AFM) using an MFP-3D AFM (Asylum Research, Santa Barbara, CA). AFM micrographs were generated using a silicon probe in AC tapping mode with a force constant of $26\,\mathrm{N\,m^{-1}}$ and resonance frequency of $300\,\mathrm{kHz}$. Photographs of etched surfaces were recorded with a $48\,\mathrm{megapixel}$ Sony Exmor IMX789 camera at a working distance of $8\,\mathrm{cm}$. Off-center lighting was maintained to maximize topographic contrast. For in-situ observations of the etch process videos were recorded with a $3\,\mathrm{megapixel}$ camera attached to a Motic SMZ140 zoom microscope. The ImageJ software package was used to

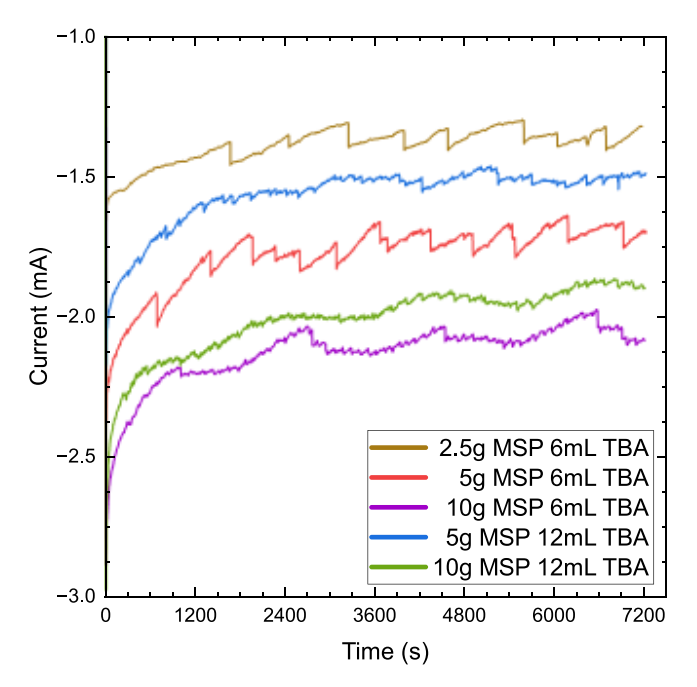


Figure 5. Etch current as a function of elapsed etch time for different additions of MSP.

extract Individual frames from the recorded video files to determine the number of observed gas bubbles per unit time and their respective diameters. Example micrographs are included in the supplemental materials.

Results

Effects of TBA.—Figure 3 shows a comparison of time-dependent etch currents with varying TBA concentration and the addition of either 5g or 10g of MSP. No stirring was employed. After initiation of the etch experiment the current rapidly decreases within the first 1200 s before it continues to decrease more gradually. Larger currents are observed for higher concentrations of MSP and lower concentrations of TBA. For all compositions sawtooth profiles, i.e., abrupt stepwise increases of current followed by more gradual decreases are observed. With increasing concentrations of TBA step wise increases in current are smaller but occur more frequently.

Figure 4 shows the calculated equivalent etch depths as a function of etchant composition. The plot includes a series of measurements for each composition alongside mean etch depths and the respective standard deviations. Increasing TBA concentration has led to a significant decrease in etch depth. Enhanced etching occurred at higher MSP concentration, while the change in etch rate with varying TBA concentration is smaller compared to the lower MSP concentration. Nominal average etch rates range between 0.053 μ m min⁻¹ and 0.066 μ m min⁻¹.

Effects of MSP.—Figure 5 shows time-dependent etch currents for varying MSP concentrations and the addition of either 6 ml or 12 ml of TBA. No stirring of the solution was employed. As observed in Fig. 3, etch currents decrease within the first 1200 s after exposure of the sample to the etchant solution. An increasing frequency for abrupt current changes is observed for increasing concentrations of MSP. Figures 3 and 5 both demonstrate negligible abrupt current changes once 12 ml of TBA are added to the etch solution. Consistent with Figs. 4, 6 demonstrates that an increase of the MSP concentration results in a statistically significant increase in etch depth, while an increase in TBA concentration leads to a decrease of etch depth for identical MSP contents. Due to the simultaneous utilization of both TBA and MSP nominal average etch rates are also between 0.053 μm min⁻¹ and 0.066 μm min⁻¹.

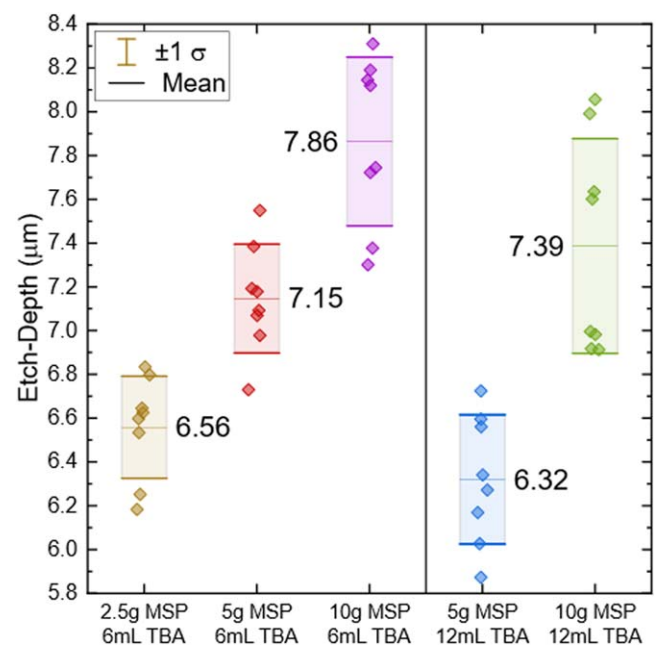


Figure 6. Volume averaged etch-depths for MSP variable experiments. Plots divided by TBA volume.

Gas bubble formation.—In-situ observation of the CE in the absence of the stir rod reveals the formation of gas bubbles on the surface of the electrode. Throughout all in-situ experiments the formation of fewer bubbles was observed in the presence of MSP. The simultaneous acquisition of video frames and electrolytic etch current reveals that abrupt changes in etch current (cf Figs. 3 and 5) coincide with the dislodgement of bubbles from the counter electrode. Table I shows the nominal number of bubbles observed at any given time during each experiment, dislodgement rates, and average bubble diameters as a function of etchant composition. Increasing the MSP concentration reduces the number of bubbles from 63 (without MSP) to 8 (5g of MSP). The dislodgement rate decreases with increasing MSP contents from 14 min⁻¹ to around 1 min⁻¹. With increasing MSP concentration, the average bubble diameter increases from approximately 0.8 mm to more than 1.7 mm. Increasing TBA concentration increased the bubble dislodgement rate and average bubble diameter, while only moderately decreasing the number of observed bubbles.

Stirring.—Figure 7 shows the effects of stirring on current as a function of time for etchants containing either 5g or 10g of MSP. Stirring decreases the transient current observed within the first 1200 s of the static experiment. For etchants containing 5g of MSP, the current stabilizes at -1.51 ± 0.02 mA for the unstirred sample, and -1.91 ± 0.01 mA when stirring is applied. For etchant solutions containing 10g of MSP currents stabilize at -1.92 ± 0.03 mA and -2.28 ± 0.02 mA in the absence and presence of stirring, respectively. Agitation of the etchant leads to a more stable current (cf Fig. 7), enhanced etch rate (Fig. 8), and increases and stabilizes the current while also reducing the average step magnitude. At 1240 rpm

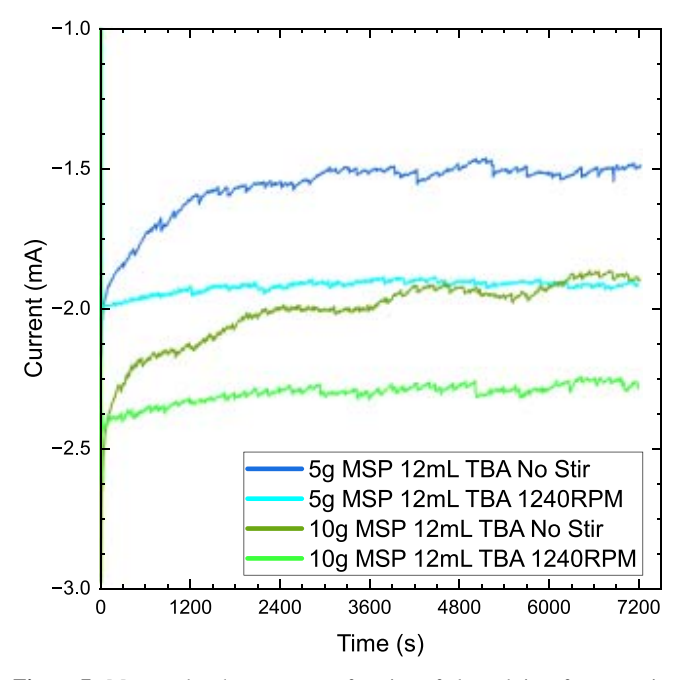


Figure 7. Measured etch current as a function of elapsed time for two pairs of etchant composition. Inclusion of stirring results in sustained \sim 0.3 mA increase in current.

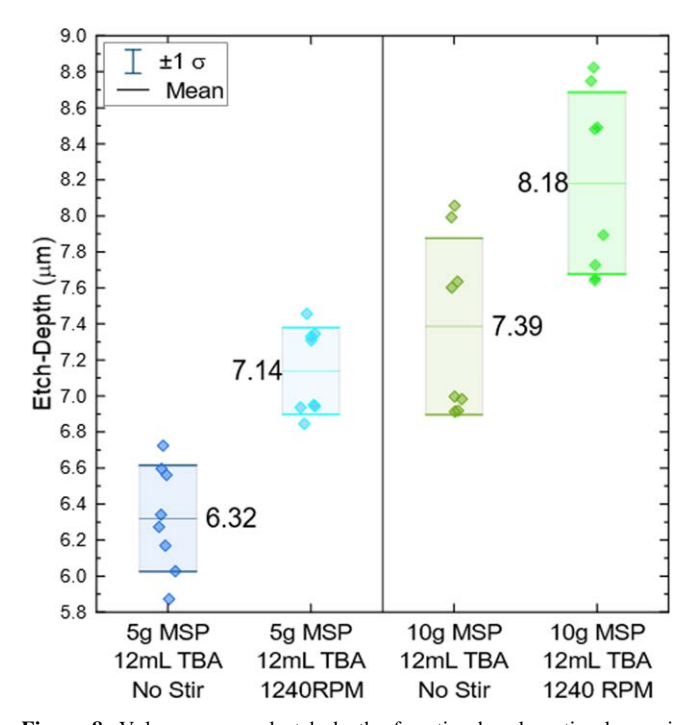


Figure 8. Volume averaged etch-depths for stirred and unstirred experiments. Plots divided by MSP mass.

Table I. Bubble statistics during in situ etching.				
	6 ml TBA 0G MSP	6 ml TBA 2.5G MSP	6 ml TBA 5G MSP	12 ml TBA 5G MSP
Bubble Count	63	27.5	8	5
Dislodgement Rate	$14.4 \; \mathrm{min}^{-1}$	$0.9~\mathrm{min}^{-1}$	$0.84 \; \mathrm{min^{-1}}$	$1.4~\mathrm{min}^{-1}$
Bubble	0.842 mm	1.145 mm	1.732 mm	1.993 mm
Diameter	±1.064	±1.343	±1.310	±1.036

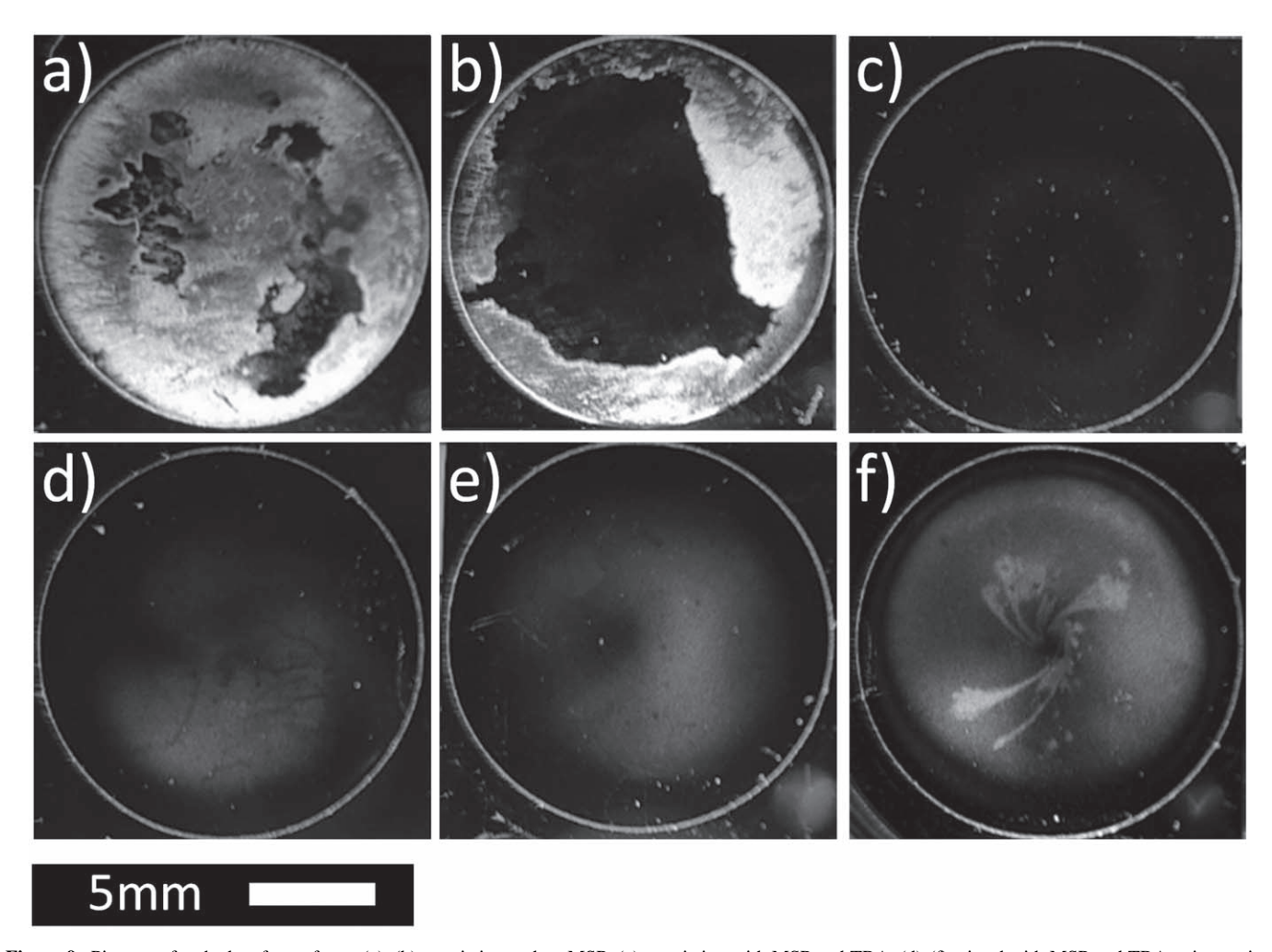


Figure 9. Pictures of etched wafer surfaces. (a)—(b) no stirring and no MSP, (c) no stirring with MSP and TBA, (d)-(f) stirred with MSP and TBA at increasing rates. Intensity of diffuse reflections correlates to surface topography. Figures share the same scale bar and are displayed in grayscale to maximize contrast.

occasional abrupt current changes around 0.021 mA were observed, similar to those in Fig. 5. For stir speeds up to 1800 rpm relatively smooth etch currents were observed. For stir speeds of 2700 rpm the etch solution becomes turbulent and the formation of a vortex inserted a steady stream of gas bubbles towards the electrodes (see Fig. S2 in supplemental materials). Nominal average etch rates during stirring were 0.060 μ m min ⁻¹ and 0.068 μ m min for 5g and 10g of MSP, respectively.

Surface characterization.—Specularity, topography, and roughness of the etched surfaces were characterized by optical microscopy, SEM, and AFM imaging, respectively. Etching without MSP or stirring created rough surfaces with a lack of specularity (Figs. 9a and 9b). The bright region in Fig. 9b was further characterized by SEM (Fig. 10b) and AFM (Fig. 10e). Pyramidal etch-pits were observed varying between 170 nm and 200 nm in depth. Stirring resulted in reduced specularity (cf Figs. 9d–9f). SEM and AFM data recorded from areas displaying diffuse light scattering revealed pyramidal features (Figs. 10c and 10f, respectively). AFM measurements revealed heights up to 100 nm above the average surface. Static etching resulted in highly specular surfaces (cf Fig. 9c) with a surface roughness of 842 pm (areal root mean square, inset of Fig. 10d).

Discussion

Effects of TBA.—Etch current and etch rate both decrease with increasing TBA contents (cf Fig. 4). The observed smaller number of gas bubbles and their higher dislodgement rate documented in Table I indicate improved wetting of the (100) germanium surface

by the etchant solution after the addition of TBA, enhancing the relative stability of the electrolyte/germanium interface. Hence, a smaller buoyant or convective force is necessary to dislodge gas bubbles from the sample surface. As a result, the effective area between the etchant and the sample surface increased which reduces masking effects. A major effect of TBA is, therefore, the homogeneity and specularity of the etched surface. The experimental findings are consistent with previous studies that have reported enhanced wetting of semiconductor surfaces after the addition of alcohols during etch experiments. ^{5,6,23} A further increase of the TBA concentration is, however, expected to cause less specular surfaces due to increased crystallographic etching anisotropy. ²³

Effects of MSP.—Increasing the MSP concentration of the etchant decreases the number of gas bubbles (cf Table I) while increasing both etch current and etch rate. The addition of phosphate ions causes complex formation with metal ions and prevents the decomposition of hydrogen peroxide. ^{21,22} The smaller availability of metal ions in the etchant limits the availability of potential nucleation sites for the formation of gas bubbles. The reduction reaction of hydrogen on the counter electrode injects electrons into the electrolyte. Hence, an increase of charge carriers in the etchant solution owing to the addition of MSP enhances the etch rate. ^{10,24,25} For negligible concentrations of MSP etching occurs primarily at local surface defects through pitting corrosion (cf Figs. 10b and 10e). The relatively low etch rates promote anisotropic etching and result in enhanced surface defects with 4-fold geometry. ^{1,18,20,24} The enhanced conductivity of the etchant due to the addition of MSP accelerates the

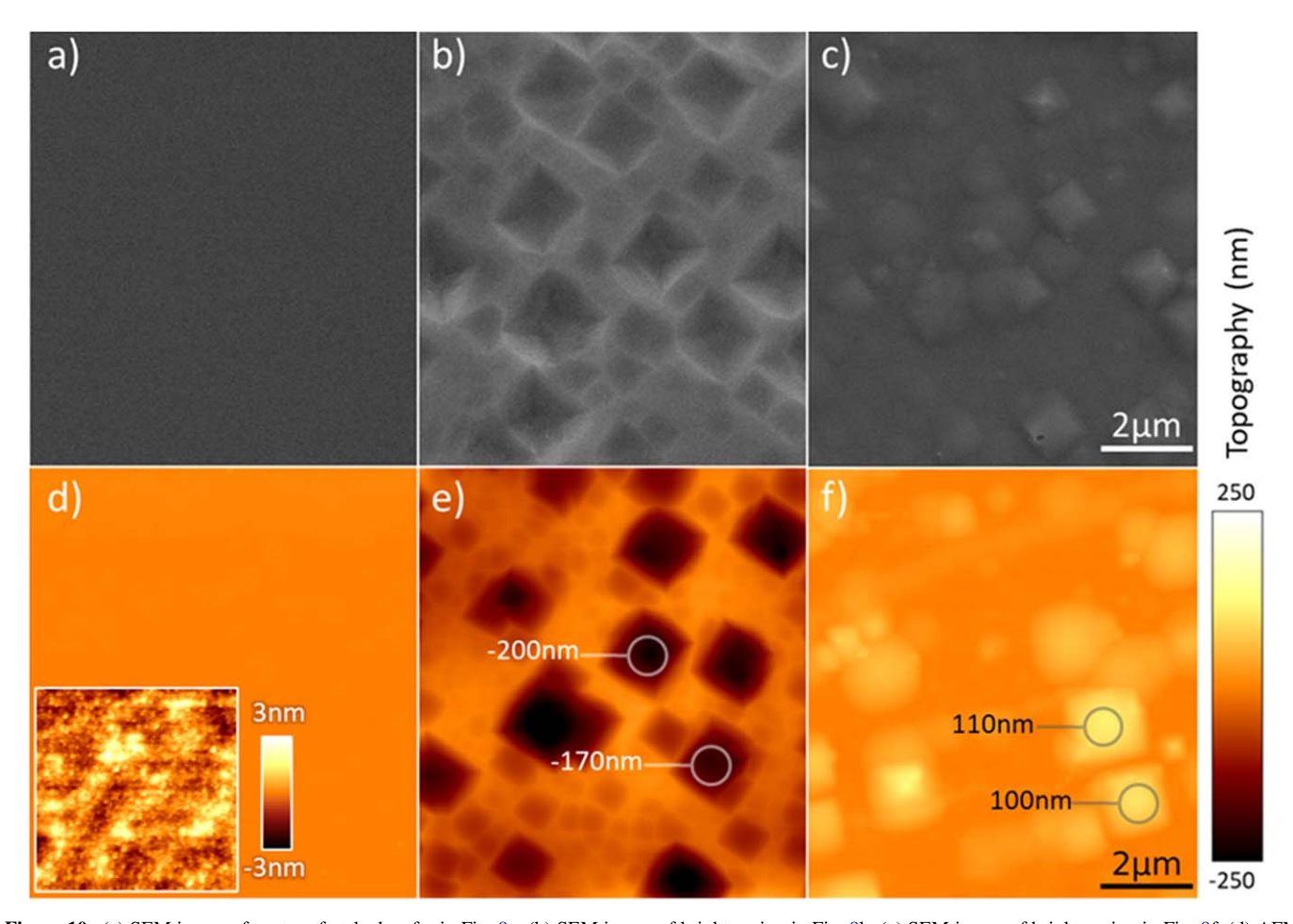


Figure 10. (a) SEM image of center of etched wafer in Fig. 9c. (b) SEM image of bright region in Fig. 9b. (c) SEM image of bright region in Fig. 9f. (d) AFM scan of center of etched wafer in Fig. 9c, Inset: same region with increased topographic contrast. (e) AFM scan of bright region in Fig. 9b. (f) AFM scan of bright region in Fig. 9f. All images and insets share the same lateral scale of 2 μ m.

oxidation reaction at the germanium surface and causes a more uniform etch front displayed by a more specular surface (cf Fig. 9c). The addition of MSP to H_2O_2 will cause formation of H_3PO_4 which can increase viscosity and alter mass transport in the solution. However, at 25 °C the expected changes in viscosity are negligible.

Effects of stirring.—Agitation of the etchant solution increases and stabilizes currents, enhances etch-rates, and decreases surface specularity (cf Figs. 7-9). The transient current decrease within the first \sim 1200 s of each experiment (cf Figs. 3 and 5) is caused by the arrangement of ions in the liquid to form an electric double layer (EDL) above the sample surface. EDLs impede charge transport towards the sample surface. ^{5,6,10,25,26} The addition of MSP increases the effective conductivity of the etchant and, thus, modifies the EDL (cf Fig. 7). The transient behavior in Fig. 7 and apparent changes of the EDL indicate the dynamic nature of electrochemical etching. A linear relationship between time and material removed is therefore insufficient to fully describe the etch behavior. However, the nominal average etch rates observed in this study reproduce those previously observed for H₂O₂-based etch solutions. ¹⁶ Agitation of the etchant reduces the effective thickness of the EDL and therefore enhances mass transport, which causes the etch process to proceed limited by the rate of the surface oxidation reaction rather than by mass transport.

Fluid flow through the etch cell acts as a mechanical force and causes dislodging of gas bubbles adhered to the sample or electrode surfaces. However, agitation above a critical stir speed causes a rotational moment imparted on the fluid to form a vortex. The consequential injection of air into the etchant disrupts the

electrochemical circuit. Moderate agitation of the etchant can minimize the impact of bubble formation on etch homogeneity and surface quality while vortex formation represents an upper limit for the stir speed. Etch cells with larger volumes or different flow mechanisms may be employed to enable utilization of higher flow rates to further decrease the width of EDLs and ensure a reaction limited etch process.

Agitation below the threshold for vortex formation leads to decreased specularity of the etched surface (cf Figs. 9f and 10c). While a relatively thin EDL maintains reaction-limited etching, a thicker EDL assists in reducing the localization of excess carriers. In the absence of a substantial EDL, surface imperfections, arising from structural defects, impurities, or other surface perturbations can act as electron-hole recombination sites and result in reduced local current densities and moderately lower etch rates. ^{10,27} Areas of lower etch rate promote the formation of pyramidal hillocks observed in Figs. 10c and 10f.

Quantification of etching.—Electrolytic etching of germanium is an oxidation reaction followed by the subsequent dissolution of the formed oxide. Myalmin et al. have proposed the following general reaction for the anodic dissolution of germanium:²⁶

$$Ge + 2.4h^{+} + 6OH^{-} \rightarrow GeO_{3}^{2-} + 1.6e^{-} + 3H_{2}O,$$
 [1]

wherein h⁺ represents holes in the valence band and e⁻ electrons in the conduction band. As germanium oxidizes, electrons from the hydroxyl groups fill the holes in the surface and create an anodic current. Within the closed electrochemical circuit, one can define the

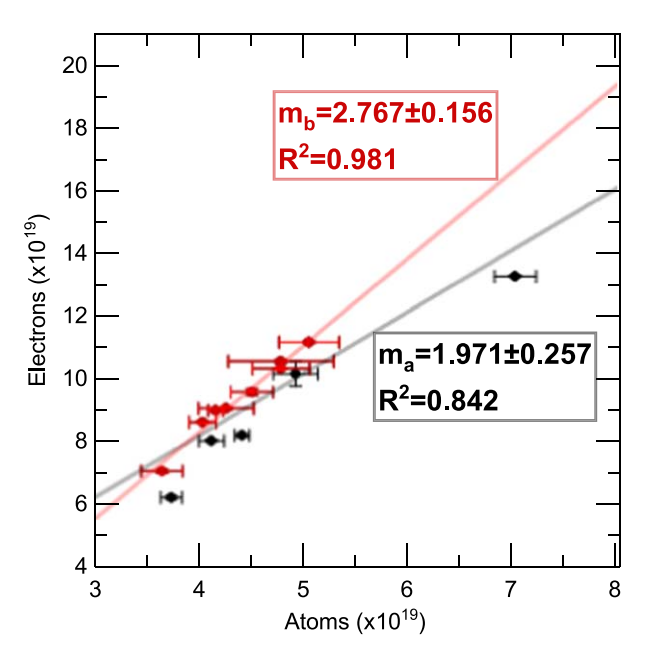


Figure 11. Calculated number of electrons transferred during the etch process as a function of material removed. The black graph with slope m_a is fitted considering all experiments with varying etching conditions. The red graph with slope m_b includes only experiments with minimal noise.

current of dissolution as either the current measured at the anode, i^a , or cathode. i^c :

$$i^a = -i^c = |i_{diss}|. ag{2}$$

A modified version of the Butler-Volmer equation relates the current of dissolution, i_{diss} , to the exchange current, i_0 , hole concentration, p_s , transfer coefficient, β , and potential drop across the EDL, $(\varphi_0 - \varphi_0^0)$ [new26]:

$$i_{diss} = -i^0 \frac{p_s}{p_s^0} e^{\beta F \left(\varphi_0 - \varphi_0^0\right)} \frac{p_s}{RT}$$
 [3]

Following Eqs. 1 and 3, the current of dissolution is directly related to the charges transferred in the electrochemical reaction. The total number of electron charges transferred over the duration of the etch process, E_c , was calculated by integrating the observed electrolytic current I for the duration of the experiment $t_f = 7200 \text{ s}$.

$$E_C = \left| \sum_{t=0s}^{t_f} I_t \right| \times 6.24E18 \, \frac{e^-}{C}$$
 [4]

 I_t is the experimentally observed current at time t (cf Figs. 3, 5, and 7). The number of atoms removed from the surface during the etch process, N, was calculated following:

$$N = \frac{\rho V_{\text{avg}}}{M_a}.$$
 [5]

 $\rho=5.323~{\rm g~cm^{-3}}$ is the density of germanium, M_a is the atomic mass, and $V_{\rm avg}$ is the average etched volume derived from the profilometry experiments. Figure 11 shows the total number of atoms removed from the germanium wafer surfaces as a function of total charges transferred during the etch experiments. The black solid line is a linear fit of all experimental data collected with a slope of $m_a=1.97\pm0.26~{\rm e^-/atom}$ and an $R^2=0.842$. The quality of the linear fit is significantly improved to $R^2=0.981$ by omission of data that were recorded from experiments during which significant gas bubble formation was observed. The red graph represents the improved linear fit with a slope of $m_b=2.77\pm0.16~{\rm e^-/atom}$.

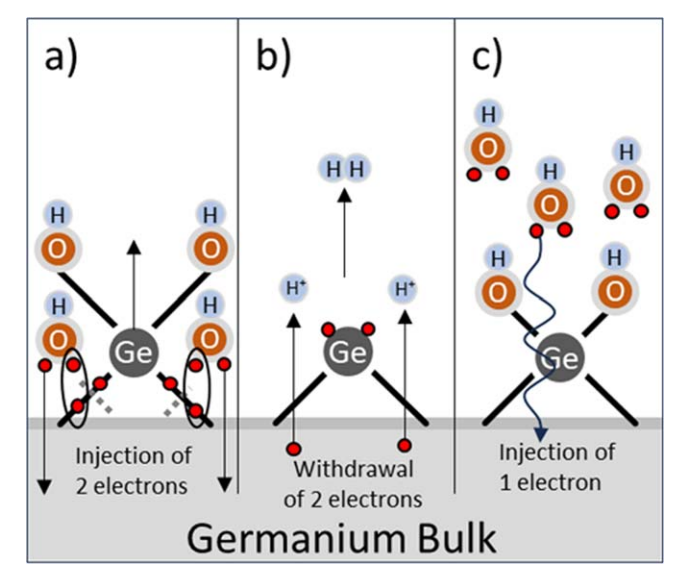


Figure 12. Diagram of select electron transfer pathways, (a) simplified sketch of the primary reaction pathway, ²⁰ (b) hydrogen gas production, and (c) leakage current in the form of electron tunneling.

The excellent linear correlation between charges transferred during the oxidation process and atoms removed from the wafer surface, independent of TBA and MSP concentrations, confirms the electrochemical nature of the etching process. The linear fit of data presented in Fig. 11 provides further insight into the underlying reaction mechanisms, confirming that the additives have a negligible impact on the chemistry of the reaction. Previous studies have described etching processes for germanium^{9,10,15,20} and silicon^{5,6,25} as redox reactions with well-known products and reactants. However, the precise reaction pathways remain largely unknown. Huygens and co-workers predict the transfer of 2 electrons for the removal of one germanium atom.²⁰ Myamlin and Pleskov²⁶ report the total transfer of 4 electrons, which is represented by Eq. 1. For silicon Seidel reports the transfer of 4 e⁻/atom with a similar mechanism,⁵ which others have previously also applied to germanium. 18 The experimental results of this study, however, demonstrate that an average of 2.77 ± 0.16 electron charges (combined holes on left and electrons on right in Eq. 1) are required to remove one germanium atom during the electrolytic etch process.

Although both linear fits displayed in Fig. 11 are characterized by relatively high R² values, the deviation from integer values shows a sensitivity of the etch process to the experimental conditions. The EDL configuration controlled by stir speed and the proliferation of bubbles both affect the accessibility of ions to the WE and alter the dominant surface reactions. The reduction of protons to hydrogen gas on the WE retrieves electrons and would have a decreasing effect on the slope observed in Fig. 11. Enhanced oxidation, i.e., formation of higher oxidation states for Ge would inject more into the WE and cause an increase of the observed slope. Figure 12 shows a sketch of the potential electron transfer pathways, including the reaction described by Huygens,²⁰ hydrogen gas production, and potential leakage current through the surface oxide and the electrolyte. The formation of hydrogen gas on the anode is unlikely, and leakage currents are considered negligible. It is therefore concluded that the formation of additional germanium oxides has increased the slope in Fig. 11 causing an overestimation of the required charge transfer to etch one Ge atom. The experimental results provide experimental evidence to support the mechanism originally proposed by Huygens²⁰ and confirm that the etch-mechanism of anodic dissolution in the presence of hydrogen peroxide differs significantly from proposals for 4-electron models.

Conclusions

This study reports electrolytic etching of germanium as a function of additives to the H₂O₂ etchant solution and etchant agitation. The

addition of TBA improves the wetting behavior of the etchant and reduces the impact of gas bubbles on the obstruction of the electrochemical circuit. The addition of MSP retards the formation of gas bubbles by preventing the decomposition of hydrogen peroxide and provides mobile charge carriers. Stirring the solution provides convective motion of the etchant to mechanically dislodge gas bubbles and minimizes the width of an electric double layer above the etch surface. A quantitative analysis of charge transfer enables direct comparison with etch rates and provides mechanistic insight to support the 2-electron mechanism of anodic dissolution of germanium in hydrogen peroxide. The observed deviation from the 4-electron mechanism used as the basis for electrolytic selectivity in silicon is critical for developing a selective etch stop for germanium. The desired control over etching of germanium will allow formation of backside imagers analogous to what is routinely obtained with silicon.

Acknowledgments

The authors appreciate invaluable discussions with Surge Mitsyuk and Dr. Cassondra Brayfield (UC Davis). Parts of the experiments were carried out at the Advanced Materials Characterization and Testing Laboratory (AMCaT) and the Center for Nano Micro Manufacturing (CNM2) at UC Davis. The Thermo Fisher Quattro Environmental Scanning Electron Microscope was funded by the NSF-MRI program (DMR-1725618). This work was performed under the auspices of the U.S. Department of Energy by Lawrence Livermore National Laboratory under Contract No. DE-AC52–07NA27344 and was supported by the LLNL-LDRD Program under Projects No. 17-ERD-050, No. 17-ERD-105, and LLNL-772753.

This article describes objective technical results and analysis. Any subjective views or opinions that might be expressed in the article do not necessarily represent the views of the U.S. Department of Energy or the United States Government.

ORCID

Charles E. Hunt https://orcid.org/0000-0003-4743-0940 Klaus van Benthem https://orcid.org/0000-0001-8865-046X

References

- 1. C. E. Hunt et al., IEEE Trans. Electron Devices, 67, 3235 (2020).
- G. F. Knoll, Radiation detection and measurement (Hoboken, N.J, John Wiley) 4th ed. p. 830 (2010).
- I. Lombardero, M. Ochoa, N. Miyashita, Y. Okada, and C. Algora, Prog. Photovoltaics Res. Appl., 28, 1097 (2020).
- P. Martín, C. Sanchez-Perez, I. García, and I. Rey-Stolle, AIP Conf. Proc., 2841, 070002 (2023).
- H. Seidel, L. Csepregi, A. Heuberger, and H. Baumgärtel, J. Electrochem. Soc., 137, 3612 (1990).
- H. Seidel, L. Csepregi, A. Heuberger, and H. Baumgärtel, J. Electrochem. Soc., 137, 3626 (1990).
- 7. S. K. Sahari et al., *Jpn. J. Appl. Phys.*, **50**, 04DA12 (2011).
- A. Garafalo, The Cleaning and Passivation of Germanium X-ray Photodiodes (University of California, Davis) (2020), (https://books.google.com/books? id=ea17zwEACAAJ).
- 9. N. Tabet, M. Faiz, N. M. Hamdan, and Z. Hussain, Surf. Sci., 523, 68 (2003).
- 0. W. H. Brattain and C. G. B. Garrett, Bell Syst. Tech. J., 34, 129 (1955).
- M. F. Ehman, K. Vedam, W. B. White, and J. W. Faust, J. Mater. Sci., 6, 969 (1971).
- 12. P. Svarnas et al., Thin Solid Films, 599, 49 (2016).
- P. Walker and W. H. Tarn, CRC handbook of metal etchants (Boca Raton, FL) (CRC Press) p. 1415 (1991).
- W. M. Klesse, G. Scappucci, G. Capellini, and M. Y. Simmons, *Nanotechnology*, 22, 145604 (2011).
- 15. S. Kagawa, T. Mikawa, and T. Kaneda, Jpn. J. Appl. Phys., 21, 1616 (1982).
- C. Sanchez-Perez, I. Garcia, and I. Rey-Stolle, Appl. Surf. Sci., 579, 152199 (2022).
- 17. L. Wang and G. Xia, arXiv:2210.08673 (2022).
- R. Divan, I. Cernica, and E. Manea, "Etch-stop in germanium induced by ion implantation for bulk micromachining applications in the IR domain." *Proc. SPIE*, *Micromachining and Microfabrication Process Technology V*, Vol. 3874, p. 403 (1999).
- 19. N. Cerniglia and P. Wang, J. Electrochem. Soc., 109, 508 (1962).
- 20. I. M. Huygens, W. P. Gomes, and K. Strubbe, ECS Trans., 6, 375 (2007).
- P. C. Wegner, Hydrogen peroxide stabilizer and resulting product and applications, US Patent 6815408B2 (2004), filed on February 6, 2003, issued November 9, 2004.
- 22. D. Jang, S. Kwon, and S. Jo, J. Propul. Power, 31, 904 (2015).
- 23. K. P. Rola and I. Zubel, Sens. Actuators, A, 242, 18 (2016).
- 24. A. Uhlir Jr, *Bell Syst. Tech. J.*, **35**, 333 (1956).
- H. Seidel, IEEE (SC, Hilton Head Island) p. 86 (1990), (https://ieeexplore.ieee.org/document/109827/).
- V. A. Myamlin and Y. V. Pleskov, *Electrochemistry of Semiconductor*, ed. V. A. Myamlin and Y. V. Pleskov (US, Boston, MA Berlin, Springer) p. 411 (1967).
- 27. S. G. Ellis, *Phys. Rev.*, **100**, 1140 (1955).